ACS OMEGA

Open Access

http://pubs.acs.org/journal/acsodf

Article

Magnetic Photocatalyst Nanocomposite Based on $MnFe_2O_4$@ZnO for AZO Dye Degradation

Javier Alonso Lopez Medina,* David Domínguez, Pedro Pizá, Guoduan Liu, Camilo Velez, Faustino Reyes Gómez, Mario Humberto Farías, Uriel Caudillo-Flores, Gerardo Soto Herrera, Hugo Tiznado, and Jorge Ricardo Mejía-Salazar

Cite This: *ACS Omega* 2025, 10, 17595−17610

Read Online

ACCESS | Metrics & More | Article Recommendations

ABSTRACT: This work focuses on fabricating a photocatalyst nanocomposite based on $MnFe_2O_4$@ZnO for degrading Red Amaranth azo dye. Manganese ferrite ($MnFe_2O_4$) magnetic nanoparticles were synthesized via a hydrothermal method, while a ZnO thin film, acting as the photoactive layer, was deposited on the magnetic cores using the atomic layer deposition (ALD) technique. X-ray diffraction (XRD) confirmed the spinel ferrite structure of $MnFe_2O_4$ and the hexagonal wurtzite phase of ZnO. The crystallite size, determined from the (311) peak, was 36.5 nm; this value was consistent with the average size of 33.2 nm measured by transmission electron microscopy (TEM). Magnetic characterization via vibrating sample magnetometry (VSM) at room temperature revealed a superparamagnetic behavior, determined by a very small hysteresis loop. The ZnO coating, achieved with 200 ALD cycles, resulted in a degradation efficiency η_{eff} of approximately 60% for the Red Amaranth dye. Finite-difference time-domain (FDTD) simulations provided theoretical insights into the electromagnetic interactions driving the photodegradation process, supporting the UV−vis absorbance data of the AZO dye. This nanocomposite can be considered as a soft magnetic material that offers promising applications in nanotechnology for environmentally friendly wastewater treatment and remediation.

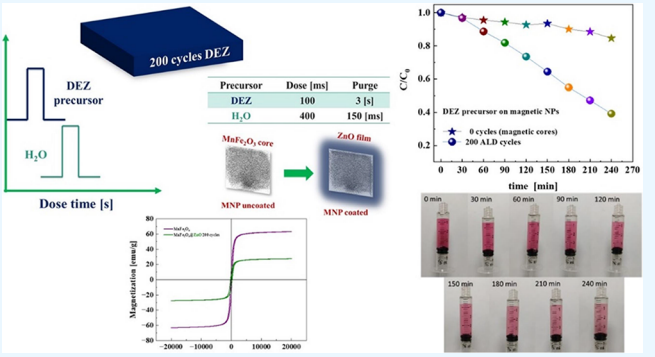

1. INTRODUCTION

Currently, rapid population growth and industrialization have caused serious impacts on the environment and human health in countries where environmental regulation policies are scarce or are not applied according to established laws. For instance, wastewater generated by dye, food, cosmetic, textile, and pharmaceutical industries discharge harmful effluents directly into the ecosystem without control.[1,2] These effluents carry numerous toxic organic substances, causing various detrimental effects on the environment, flora, and aquatic fauna.[3] These effects can have significant consequences, such as reduction in dissolved oxygen levels in water, formation of persistent and toxic compounds harmful to aquatic organisms living in freshwater sources used for human consumption, obstruction of light penetration into the water bodies, among others.[4,5] Furthermore, organic pollutants can also harm human health by being carcinogenic, teratogenic, mutagenic, and interfering with the endocrine system.[6−13] Nowadays, there are multiple techniques applied in the decontamination of wastewater, including electrodialysis, membrane filtration, precipitation, adsorption, electrochemical reduction, and electro-deionization.[14−20] However, these processes often consume large amounts of energy and present complications in transferring contaminants between different fluids and generating by-products during treatment.[21,22] Therefore, it is of great importance to develop environmentally friendly, cost-effective, and highly efficient methods for wastewater treatment. For instance, heterogeneous photocatalysis has been widely studied and applied in various areas such as water purification, CO_2 reduction, and N_2 fixation. This method can degrade organic contaminants in wastewater and transform them into carbon dioxide, water, or other small molecules.[22−28]

It is known that nanotechnology plays an important role in generating knowledge at the applied level to resolve real problems that affect society, especially in vulnerable populations exposed to contaminated water consumption.[29,30] Thus, the new knowledge involves understanding different

Received: December 20, 2024
Revised: March 12, 2025
Accepted: April 17, 2025
Published: April 26, 2025

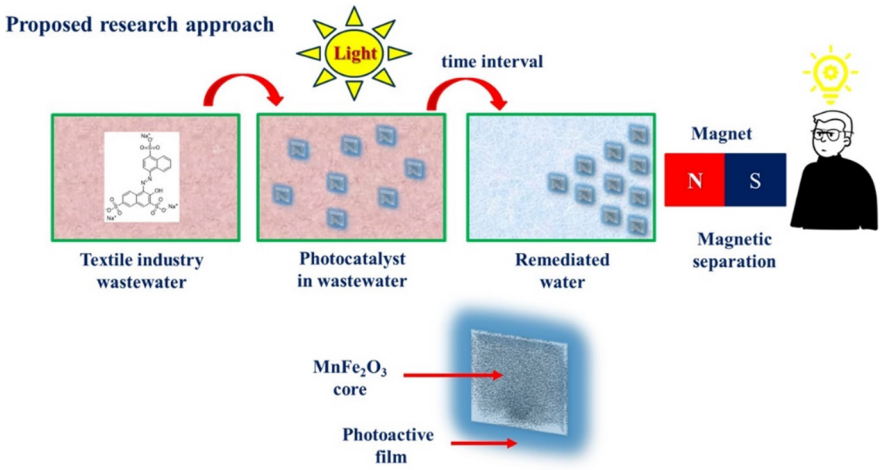

Figure 1. Schematic overview of the proposed research approach.

topics related to synthesis processes in new materials, modifying and controlling their physical and chemical properties, and their potential applications according to the needs of the industry and society. With the knowledge gained in fabrication methods, nanostructures have been prepared for specific desired applications by controlling their magnetic, electrical, optical, thermal, electronic, or mechanical properties.[31−33] These types of nanostructures can be referred to as "functional nanostructures", and the stimulus-response relationship is key in determining the field of knowledge in which they can be employed. In this context, there is concern about modifying the physical and chemical properties of nanostructures when combining materials of different nature or behavior, generating more than one physical response in the material.[34−37] The combination of magnetic properties of magnetic cores with the optical response associated with a semiconductor material allows the development of so-called magnetically controlled multifunctional materials that can be applied in fields such as photocatalysis for water treatment.[38−41] The magnetic properties of different materials can be of particular interest due to the possibilities of external manipulation by the application of external magnetic fields. This is the case with spinel-type ferrites MFe_2O_4, where M can be a transition element (a cation of Co, Ni, Fe, Mn, or Zn with different stoichiometry). These ferrites are characterized by high chemical stability, magnetic behavior intimately linked to their dimensionality, biocompatibility, and their ability to absorb or emit radiation over a wide range of the electromagnetic spectrum (UV−vis-NIR).[42,43] Such ferrites have exhibited interesting properties as multifunctional materials when these are combined with a photoactive material that allows them to be used in photocatalytic tests to degrade contaminants and to be able to be separated magnetically with an external field using a conventional magnet.[38,44−47] In addition, multiple types of catalysts can be employed in photocatalytic processes based on ferrites with different crystal structures, such as spinel, garnet, magnetoplumbite, or orthoferrite. These kinds of materials are characterized by being oxides containing Fe^{3+} and at least another metal cation (transition metal), which have been applied as powders, films, or ceramics. The photocatalyst based on magnetic ferrites has attracted great interest and has quickly become a trending topic among scientists, as reflected in the increasing number of publications per year in the last 8 years, from less than 10 to more than 40.[48−50]

Many researchers have utilized ferrite photocatalysts for degrading organic pollutants. Ramadoss et al., in 2020,[51] synthesized magnetic nanoparticles of $MnFe_2O_4$ for the photocatalytic degradation of Congo Red dye under visible light. In degradation studies conducted using a photoreactor with irradiation in the range of 565 nm, approximately 98.3% of the dye was successfully mineralized and transformed into nontoxic alcohols and acids.[52] Furthermore, due to the magnetic nature of the nanoparticles, they could be easily recovered and utilized in multiple cycles. Taghavi Fardood et al., in 2019,[53] tried the malachite green dye photodegradation from the synthesis of magnetic nanoparticles based on $MgFe_2O_4$. They found that the obtained nanoparticles exhibited superparamagnetic behavior as well as high photocatalytic activity under visible light irradiation. They were able to degrade the malachite green dye up to 98% and took advantage of the magnetic response of the ferrite to carry out different repetition cycles, recycling the nanoparticles through magnetic separation processes. Rodiah and Ditiyaningrum, in 2022,[54] performed the green synthesis of a photocatalyst based on $NiCoFe_2O_4$ nanoparticles. They used these nanoparticles to perform photodegradation for 300 min under UV light of diazinon, an organophosphate insecticide used to control insects in the soil, in ornamental plants, and fruit and vegetable crops, reaching a percentage degradation of 72.4% using 12 mg of catalyst.

Wang et al., in 2016,[55] studied the photodegradation of Rhodamine B dye using magnetic nanoparticles of Fe_3O_4 coated with ZnO as a core−shell structure catalyst. In this case, after Fe_3O_4 nanoparticles were synthesized via the chemical coprecipitation method, a ZnO coating was added through the hydrothermal method. They found that this core−shell structure in aqueous solution under ultraviolet light achieved a 99.3% degradation of Rhodamine B, taking only 60 min. Also, they found that larger-sized nanoparticles presented better catalytic activity. This was attributed to the fact that the concentration of surface oxygen vacancies is a vital factor for photocatalytic performance. The advantage of the core−shell structure was highlighted, as it exhibited a higher percentage of efficiency in dye degradation compared to using only photocatalytic material, in addition to facilitating its recovery and subsequent reuse.

https://doi.org/10.1021/acsomega.4c11468
ACS Omega 2025, 10, 17595−17610

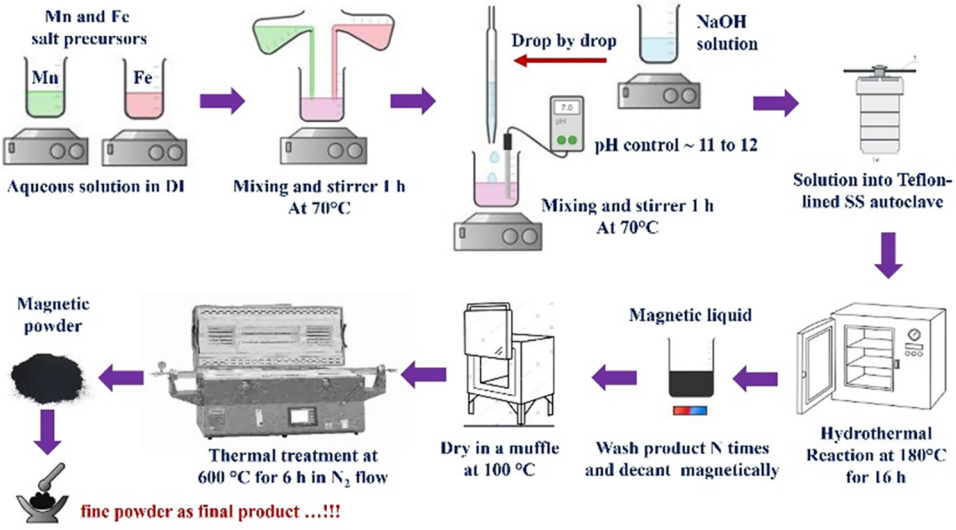

(a)

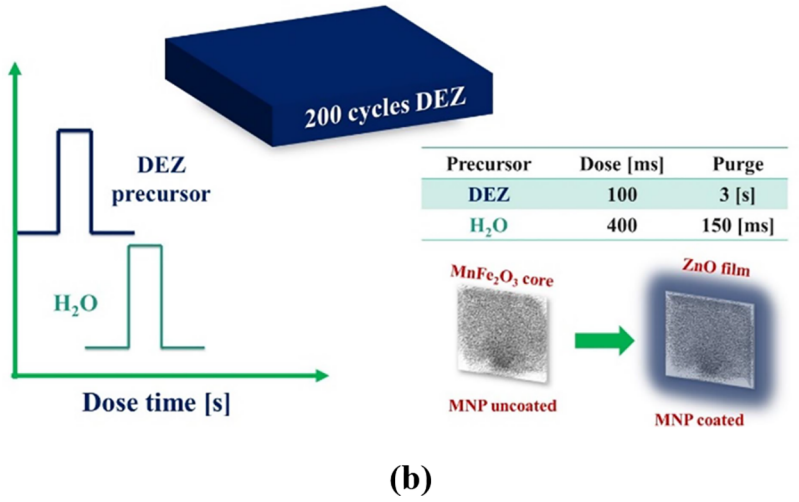

(b)

Figure 2. Nanoomposite material scheme fabrication (a) $MnFe_2O_4$ magnetic cores synthesis by hydrothermal method and (b) $MnFe_2O_4$@ZnO nanocomposite by the ALD process to be coated with ZnO as the photoactive material on the magnetic cores surface.

In this work, we consider the problems of the presence of azoic dye in wastewater that is discharged by the textile, food, dye, and pharmaceutical industries. Photoactive ZnO thin films with different thickness values were grown over magnetic nanoparticles via atomic layer deposition (ALD). Since one of the objectives was to prepare a nanocomposite material that could be easily recovered from aqueous solutions using a conventional magnet, as shown in Figure 1, the magnetic core photocatalyst $MnFe_2O_4$@ZnO was prepared via a hydrothermal method for AZO dye degradation, combining two synthesis techniques in synergy to create a multifunctional material. This material integrates the magnetic properties of ferrites with the photoactive characteristics provided by a ZnO thin film coating.[38] Studied samples were widely characterized and applied in the photocatalytic degradation of toxic Red Amaranth azo dye.

2. EXPERIMENTAL SECTION

2.1. Magnetic Core Photocatalyst Fabrication. The preparation of the nanocomposite material involves two main stages, each meticulously optimized to achieve the desired properties and performance in the final product. First, $MnFe_2O_4$ magnetic powders are synthesized via the hydrothermal method, where precursor materials are exposed to controlled temperature and pressure within a hydrothermal reactor,[56,57] forming the desired magnetic powder.[58] Next, a ZnO layer is applied to the magnetic nanoparticles using ALD.[59−61] This technique allows for highly precise, atomic-level conformal coatings, resulting in a uniform ZnO layer on the $MnFe_2O_4$ nanoparticles. As ZnO is a well-known semiconductor with photocatalytic properties,[62] this layer enhances the nanocomposite's functionality. Figure 2a,b provides a schematic overview of the fabrication process for $MnFe_2O_4$ magnetic nanoparticles and $MnFe_2O_4$@ZnO nanocomposites.

2.1.1. Magnetic Nanoparticle Synthesis. The magnetic cores were fabricated using the hydrothermal synthesis method described by Kafshgari et al. in 2018,[63] as shown in Figure 2a. In our experiment, we dissolved $Fe(NO_3)_3$-$9H_2O$ and $Mn(NO_3)_2$-$4H_2O$ in deionized water, creating an aqueous

https://doi.org/10.1021/acsomega.4c11468
ACS Omega 2025, 10, 17595−17610

solution (metal salts were purchased from Sigma-Aldrich). The two solutions were mixed and stirred using a hot plate with a magnetic stirrer until complete dissolution of the reactants. While stirring, a NaOH solution was gradually added dropwise until reaching a desired pH, and the reaction temperature was maintained at 70 °C for 1 h. Subsequently, the resulting solution was transferred to a Teflon-lined hydrothermal autoclave reactor. The reactor was placed in an oven and heated at 180 °C for 16 h to promote the magnetic core formation. Once the reaction time was completed, the product was cooled to room temperature. To remove any impurities, the mixture was washed multiple times with absolute ethanol via magnetic decantation and dried in an oven to eliminate any remaining ethanol present. Next, the material was ground to a fine powder using an agate mortar, and 735.8 mg of dark brown magnetic powder was obtained. Finally, the $MnFe_2O_4$ magnetic powder was calcined at 600 °C for 6 h under UHP N_2 inert atmosphere.

2.1.2. Photoactive Material Growth by ALD. The obtained fine powder, described above, was coated with a ZnO layer by means of the ALD technique, as shown in Figure 2b. For the ALD coating, the used precursors were diethylzinc (DEZ) as organometallic precursors at room temperature (Growth Per Cycle, GPC = 1.8 Å/c) and deionized water as a reactant agent.[38,61] The ALD process was carried out in a Beneq model TFS 200 system, with a reactor temperature of 150 °C. N_2, purified to $<10^{-12}$ ppm of O_2, was utilized as carrier/purging gas during the entire process. The experimental setup has been documented in our previous works.[38] In this case, 20 mg of magnetic powder was placed on a metal plate. On the rear of the plate, there is a matrix of nine Sm−Co permanent magnets, 5 mm in diameter, to avoid the magnetic material being pulled out by the mechanical pump to the outside of the ALD reactor during the coating process. Additionally, Si (100) substrates were placed within the reactor and on the metal plate as control samples to measure the layer thickness via the ellipsometry technique. The plate was situated at the entry point for precursors into the reactor chamber, where the ALD process was executed over 200 cycles, resulting in a coating thickness of approximately 36 nm, as estimated from ellipsometry. The ALD process to prepare the ZnO layer consists of the following sequence of pulses: 1 pulse of the DEZ precursor with 25 ms dose and 1 pulse of the H_2O DI with 50 ms dose per cycle, with a purge time of 3 s for both precursors. The sequence described above is repeated 200 times to obtain the desired thickness described above. As mentioned earlier, the thicknesses for the ZnO coat were obtained by spectroscopic ellipsometry at room temperature by taking measurements on the Si control sample. Also, the $MnFe_2O_4$@ZnO nanocomposite was calcined under the same temperature, annealing time, and N_2 inert atmosphere.

Figure 2 depicts the nanocomposite fabrication scheme based on $MnFe_2O_4$ magnetic cores coated with ZnO as the photoactive material.

In this study, we used atomic layer deposition (ALD) for coating $MnFe_2O_4$ magnetic nanoparticles due to its ability to provide precise thickness control, excellent uniformity, strong adherence, and high-purity ZnO films. These characteristics make ALD the preferred technique when ultrathin and high-quality coatings are required. Several deposition techniques, including magnetron sputtering, laser ablation, and spray pyrolysis,[64,65] have been employed for ZnO thin film synthesis. However, sol−gel and hydrothermal synthesis methods are commonly used since they are cost-effective and easy to implement.[65] Despite these advantages, sol−gel and hydrothermal approaches present significant challenges in achieving homogeneous ultrathin films, particularly on complex nanostructured surfaces.[66,67] Moreover, only a few studies have reported successful deposition of ZnO ultrathin films onto $MnFe_2O_4$ magnetic nanoparticles in powder form using sol−gel or hydrothermal synthesis. In contrast, ALD is a widely used technique for depositing conformal ultrathin films on powdered materials, including magnetic nanoparticles with a high surface area and complex geometries, with promising applications in the photocatalysis field. Additionally, ZnO films synthesized via the sol−gel method typically require a postdeposition thermal treatment to achieve crystallization.[68] On the other hand, the hydrothermal synthesis process can induce crystallization during the reaction, although in some cases, an additional thermal treatment enhances the material's properties. In contrast, the ALD technique enables the deposition of ZnO films in the crystalline phase at a reactor temperature of 200 °C, eliminating the need for a postdeposition thermal treatment.[38,69]

2.1.3. AZO Dye Preparation. The dye used in this work was Red Amaranth, from Sigma-Aldrich (CAS number: 915-67-3), and empirical formula $C_{20}H_{11}N_2Na_3O_{10}S_3$. Red Amaranth is valued for its ability to produce intense reddish tones, making it a popular choice for coloring textiles, food products, cosmetics, and pharmaceuticals.[7,70] Its AZO-bond (−N═N−) (see Figure 3) gives it stability and bright coloring facts,

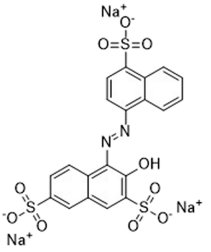

Figure 3. Organic molecule of Red Amaranth scheme[70] (also known as E123) with empirical formula $C_{20}H_{11}N_2Na_3O_{10}S_3$ and characterized by AZO Group (−N═N−), Aromatic Rings, Sulfonic Acid Groups ($-SO_3H$) and Sodium Salt. This figure was adapted from the National Center for Biotechnology Information (2025), PubChem Compound Summary for CID 13506, Amaranth. Retrieved April 15, 2025, from https://pubchem.ncbi.nlm.nih.gov/compound/Amaranth.

which have contributed to its extensive use in the industry. However, despite its widespread application, Red Amaranth has raised significant health and environmental concerns. Classified as a potentially toxic dye, it has been linked to various adverse effects on human health.[7] For the photocatalytic experiment, the Red Amaranth dye solution was prepared and placed in a cylindrical quartz cell inside the reactor with a total volume of 250 mL at a concentration of 20 ppm.

2.2. Numerical Simulations. The finite-difference time-domain (FDTD) simulator from commercial Lumerical research software was utilized to model the scattering, absorption, and extinction efficiencies of $MnFe_2O_4$ and $MnFe_2O_4$@ZnO nanoparticles. The FDTD method operates by discretizing time-dependent Maxwell's equations in both space and time, utilizing central differences to approximate partial derivatives. The shape and size of the nanoparticles

https://doi.org/10.1021/acsomega.4c11468
ACS Omega 2025, 10, 17595−17610

were determined through TEM studies, while their optical indices were sourced from previous studies.[71,72] A total-field scattered-field (TFSF) light source was employed, covering a wavelength range from 250 to 800 nm. To achieve high accuracy, a grid resolution of 0.2 nm was used. The absorption cross-section was calculated by positioning a cross-sectional analysis group within the TFSF source, whereas the scattering cross-section was determined using a similar analysis group placed outside the source. The extinction efficiency was subsequently obtained as the sum of the scattering and absorption efficiencies. To analyze the electric field distribution, a frequency-domain field monitor was positioned around the TFSF source. The surrounding medium was assumed to be water, with a refractive index of 1.33. The simulation region was enclosed by a Perfectly Matched Layer (PML) to minimize boundary reflections and ensure accurate results.

2.3. Characterization. The produced magnetic nanoparticles (NPs), with and without a ZnO coating, were subjected to various characterization techniques to obtain detailed information on their size distribution, morphology, crystalline structure, magnetic response, and photodegradation capacity of the Red Amaranth dye.

Morphological properties and size distribution for magnetic NPs were recorded in a JEOL JEM-2100F high-resolution transmission electron microscope (STEM) using an accelerating voltage of 200 and 400 kV, respectively. This microscope is equipped with an energy-dispersive X-ray spectroscopy (EDS) module for chemical mapping analysis. For TEM measurements, a small amount of fine powder was dispersed in ethanol to minimize the magnetic aggregates present in the carbon-coated copper grid (400 mesh). A small portion of the solution was dropped onto the copper grid and dried at room temperature before the characterization process.

The textural properties were characterized through N_2 physisorption analysis by using a Micromeritics Tristar-II 3020 physisorption analyzer. The samples were pretreated under vacuum at 300 °C for 3 h using a sample degassing system (VacPrep-061) from Micromeritics Instruments. The textural properties were calculated from adsorption−desorption isotherm data, measured within the relative pressure (P/P_0) range of 10^{-5}−0.995. The specific surface area, pore volume, and pore size distribution of each solid were determined by using the classical Brunauer−Emmett−Teller (BET) method (Sing, 2014) and the Barrett−Joyner−Halenda (BJH) method (Barrett, Joyner, and Halenda, 1951).

The crystalline structure of the studied samples was obtained using a PANalytical X'Pert PRO diffractometer (CuK_α radiation with $\lambda_{CuK\alpha}$ = 1.5418 Å). Before characterizing, the magnetic photocatalyst nanocomposite was annealed at 600 °C for 3 h under a nitrogen atmosphere to avoid oxidation and subsequent formation of undesired crystalline phases. The diffractogram was registered in the 2θ range 10°-80° using a step size and dwell time of 0.02° and 0.5 s, respectively, and the patterns were compared to the ICSD (Crystal Structure Database) from HighScore Plus. Finally, from X-ray diffraction patterns, the structural parameters and crystal size for magnetic cores ($MnFe_2O_4$) and magnetic nanocomposite $MnFe_2O_4$@ZnO were determined.

The magnetic response of the $MnFe_2O_4$ and $MnFe_2O_4$@ZnO nanoparticle samples in dry powders was evaluated by vibrating sample magnetometry -VSM (MicroSens MicroSense EZ9HF), which allows determination of fundamental magnetic properties relevant for potential process applications, such as coercivity, saturation, and magnetic remanence. The hysteretic magnetization loop was measured at room temperature by varying the applied field between −20,000 and 20,000 Oe.

Thickness for the ZnO layers was obtained through spectroscopic ellipsometry (SE) at room temperature using a Spectroscopic Ellipsometer (VASE), J.A. Woollam Co. The required ellipsometric parameters (Ψ and Δ) for SE analysis were recorded in the wavelength spectral range from 240 to 1000 nm at four different incidence angles 45, 55, 65, and 75°. SE measurements were performed in the witness silicon substrates placed in the reactor and on the metallic plate located next to the magnetic powders.

Photodegradation experiments were achieved using magnetic nanoparticles coated with ZnO as photocatalysts to decompose the Red Amaranth dye. The dye solution was irradiated with UV−vis light, and the degradation process was monitored over time. Photodegradation efficiency was evaluated by comparing the performance of nanoparticles with and without the ALD coating. The Red Amaranth dye was subjected to photodegradation using a Rayonet photochemical reactor (model RPR 100), equipped with 16 lamps emitting at wavelength λ_{uv} = 250 nm. The experiment was accomplished with sampling intervals every 30 min until a total of 240 min. Dye degradation was assessed by measuring absorbance at 520 nm, corresponding to the characteristic absorption peak of this azo dye, in a Cary 50 UV−vis spectrophotometer at room temperature using a 4 mL quartz cuvette for sampling.

3. RESULTS AND DISCUSSION

3.1. Structural Studies. An X-ray diffractogram is used to confirm nanoparticle crystal structure and crystallite size; Figure 4 presents XRD patterns of two samples: magnetic $MnFe_2O_4$ powder (purple line) and $MnFe_2O_4$@ZnO nanocomposite (green line). The diffractogram reveals distinct Bragg peak reflections at specific θ-2θ positions for both $MnFe_2O_4$ and $MnFe_2O_4$@ZnO. For $MnFe_2O_4$, characteristic Bragg peaks were observed at 17.93, 29.73, 32.88, 34.73, 42.85, 52.31, 55.98, 61.47, 72.77, and 88.76°, corresponding to the

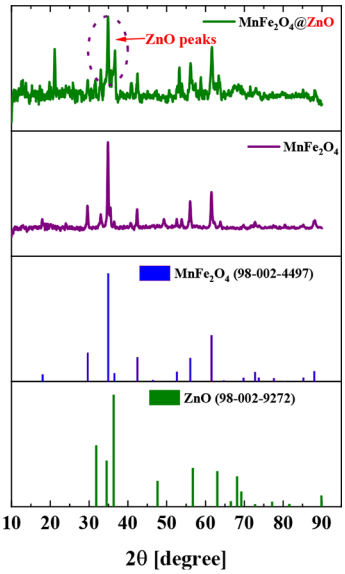

Figure 4. XRD pattern for $MnFe_2O_4$ magnetic nanoparticles and the $MnFe_2O_4$@ZnO nanocomposite.

https://doi.org/10.1021/acsomega.4c11468
ACS Omega 2025, 10, 17595−17610

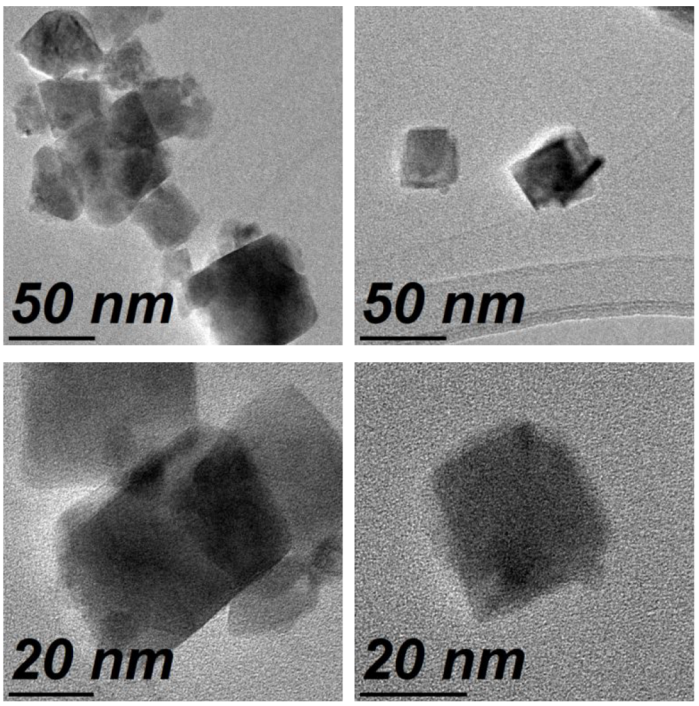

(a)

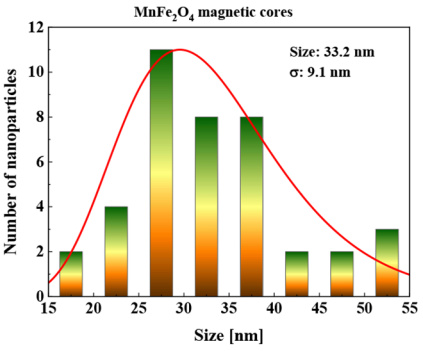

(b)

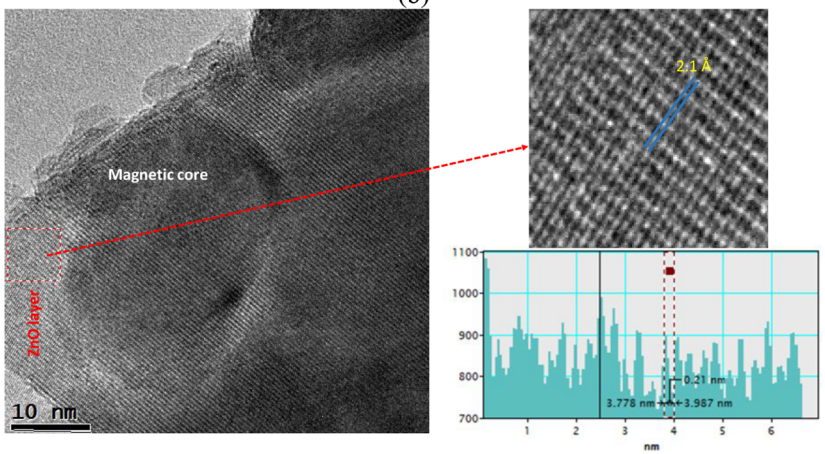

(c)

Figure 5. TEM and HR-TEM micrographs of $MnFe_2O_4$ magnetic nanoparticles and $MnFe_2O_4$@ZnO nanocomposite. (a) Micrographs show cubic morphology of studied nanoparticles at the 50 nm scale (above) and 20 nm scale (below). (b) Particle size distribution of $MnFe_2O_4$ cores before ZnO coating via ALD. (c) High-resolution and inset images (marked and highlight in red dashed lines) show crystalline zones of ZnO coating and well-defined crystalline structure of magnetic cores.

crystallographic planes (111), (220), (311), (222), (400), (422), (511), (440), (533), and (731). These reflections are consistent with a face-centered cubic (FCC) phase, typical of a normal spinel structure, and are indexed to the space group Fd3m, as corroborated by the ICSD reference file No. 98-002-4497.

https://doi.org/10.1021/acsomega.4c11468
ACS Omega 2025, 10, 17595−17610

In the $MnFe_2O_4$@ZnO nanocomposite, similar Bragg peak positions are observed at θ-2θ angles corresponding to the crystallographic planes of the $MnFe_2O_4$ magnetic core, confirming the presence of a normal spinel structure for manganese ferrite. In addition, new peaks appear, attributable to the wurtzite structure of ZnO (slightly overlapped with characteristic peak of spinel structure for magnetic cores), with reflections observed at θ-2θ positions 31.63, 34.91, 36.69, 47.41, 56.25, 63.37, 68.43, 72.95, 77.33, and 88.09°. These reflections correspond to the crystallographic planes (010), (200), (110), (210), (011), (310), (211), (400), (220), and (320) of ZnO. The wurtzite structure is confirmed by its space group P63mc, as indicated by ICSD reference file No. 98−002−9272. The presence of these ZnO peaks verifies the successful deposition of ZnO coating on the magnetic nanoparticles via ALD.

Using the Debye−Scherrer equation, the average crystallite size of the $MnFe_2O_4$ nanoparticles[73] was estimated to be approximately 36.5 ± 0.2 nm, based on the XRD data. Furthermore, a shift in the XRD peaks toward higher diffraction angles is observed in the diffractograms of the powder materials. This shift, commonly referred to as a high-angle shift, indicates a reduction in crystallite size, which is typically induced by the high-temperature calcination process used during synthesis. As crystallite size decreases, the number of atoms per crystallite also diminishes, which subsequently affects the overall particle size of the powdered materials, also, the crystallite size is determined by factors such as the synthesis method, calcination conditions, and the intrinsic properties of the material.[74] While a peak shift toward higher angles provides indirect evidence of reduced crystallite size, further complementary characterization techniques, such as TEM, are essential to fully elucidate the morphology and nanostructure of the fabricated materials.

3.2. Morphological Studies. A TEM micrograph of $MnFe_2O_4$ and $MnFe_2O_4$@ZnO nanoparticles is presented in Figure 5. In Figure 5a, it is possible to observe well-defined grains agglomerated with cubic morphology, characterized by their uniform and consistent shape. The nanoparticle size was analyzed using ImageJ, an open-source software for processing and analyzing scientific images, revealing that the magnetic cores without a ZnO layer have an average size of around 33.2 ± 0.2 nm. The size distribution was fitted using a log-normal distribution function type, as shown in Figure 5b. In addition, Figure 5c exhibits small monocrystalline domains in the magnetic cores, indicating the high crystallinity present in the material. Also, there are crystalline zones associated with the ZnO film growth via ALD. The inset figure at the right of Figure 5c shows the inverse fast Fourier transform (IFFT) calculated from HR-TEM images of the region highlighted by red squares. IFFT results allowed us to obtain information about the planar distance, diameter, and crystallinity degree for the sample. A continuous, black and bright, well-defined fringe can be observed, indicating the highly crystalline nature of the NPs and the ZnO film.

According to these analyses, the hydrothermal method allows us to obtain $MnFe_2O_4$ magnetic nanoparticles with well-defined cubic geometry. Therefore, it was chosen to fabricate magnetic nanoparticles due to their ability to yield uniform and dispersed nanoparticles with controlled morphology. It enables precise regulation of reaction parameters such as temperature, pressure, and reaction time, thereby facilitating the production of high-purity materials and well-defined particle sizes, typically within the nanometer to micrometer range. In addition, the presented morphological and size results are in good agreement with DRX crystallite size and magnetic behavior studies from the hysteresis loop, confirming that the magnetic NPs could be considered a soft magnetic material, which is easily magnetized and demagnetized under an external magnetic field.

The presence of cubic-shaped grain aggregates indicates effective control over particle nucleation in the fabrication process, demonstrating that the synthesis of tailored nanostructures was designed successfully. This precise control over morphology and particle distribution could enhance nanocomposite performance in various technological applications, such as in heterogeneous photocatalysis, which involves magnetic materials coated with semiconductor films for environmental remediation. Additionally, Figure 6 presents

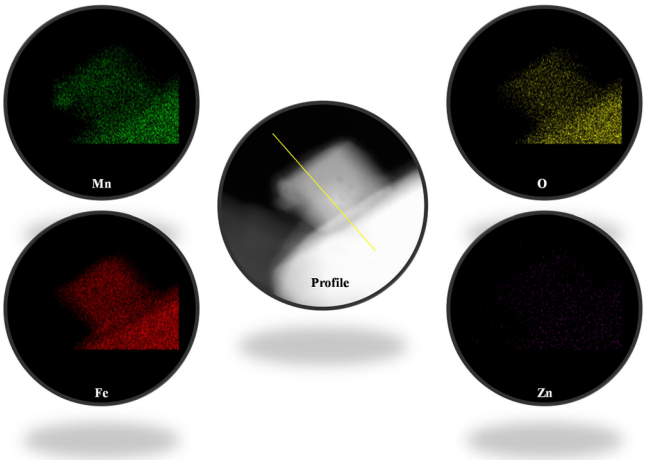

Figure 6. Chemical mapping of the $MnFe_2O_4$@ZnO nanocomposite. The STEM-EDS elemental maps illustrate the spatial distribution of the constituent elements within the material. The central image represents the region from which the STEM-EDX spectra were acquired. The elemental distribution is depicted using false-color representation as follows: Mn (green), Fe (red), O (yellow), and Zn (violet).

STEM-EDS elemental mapping of $MnFe_2O_4$@ZnO nanocomposite, displaying a pseudocolor image generated from transmitted electrons corresponding to nanoparticles along the selected profile line scan (shown in the central image). The green color represents the X-ray emission from Mn−K, indicating the distribution of manganese atoms within the magnetic core. The red color corresponds to Fe K emission, revealing the presence of iron within the nanoparticles. The yellow color indicates the emission of O−K, associated with oxygen in the ferrite, while the violet color represents Zn−K emission, reflecting the distribution of zinc atoms on the magnetic nanoparticles, deposited via the ALD method. This elemental analysis demonstrates a uniform distribution of transition metals and the photoactive ZnO material throughout the $MnFe_2O_4$@ZnO nanocomposite, synthesized via the hydrothermal method and subsequently coated with ZnO. This consistent elemental distribution confirms the successful fabrication of the nanocomposite material.

3.3. BET Measurement. The surface area of a photocatalyst is a critical parameter that significantly influences its photodegradation performance as it directly affects the

https://doi.org/10.1021/acsomega.4c11468
ACS Omega 2025, 10, 17595−17610

availability of active sites for photocatalytic reactions. Table 1 relates the textural and surface properties of the materials

Table 1. Textural Properties (BET Specific Surface Area, Pore Volume, and Average Pore Size) of a Magnetic Photocatalyst Nanocomposite Based on $MnFe_2O_4$@ZnO

catalyst	BET surface area [$m^2\ g^{-1}$]	pore volume [$cm^3\ g^{-1}$]	pore size [nm]
$MnFe_2O_4$	35.6	0.101	21.2
$MnFe_2O_4$@ZnO	16.2	0.069	14.2

(specific surface area (A_{BET}), pore volume, and average pore size) obtained by N_2 physisorption analysis. As is appreciated, A_{BET} decreases from 35.6 $m^2\ g^{-1}$($MnFe_2O_4$) to 16.2 $m^2\ g^{-1}$ ($MnFe_2O_4$@ZnO), pore volume from 0.101 $cm^3\ gr^{-1}$ ($MnFe_2O_4$) to 0.069 $cm^3\ gr^{-1}$ ($MnFe_2O_4$@ZnO), and average pore size from 21.2 nm ($MnFe_2O_4$) to 16.2 nm ($MnFe_2O_4$@ZnO). This considerable decrease in the textural and surface properties of the $MnFe_2O_4$@ZnO photocatalyst is attributed to the ZnO thin film deposited on magnetic-supported material, as has been confirmed by TEM characterization.

3.4. Magnetic Properties. Magnetization (M) as a function of the magnetic field (H) measurements at room temperature for $MnFe_2O_4$ nanoparticles and $MnFe_2O_4$@ZnO nanocomposite are shown in Figure 7. A small hysteresis loop

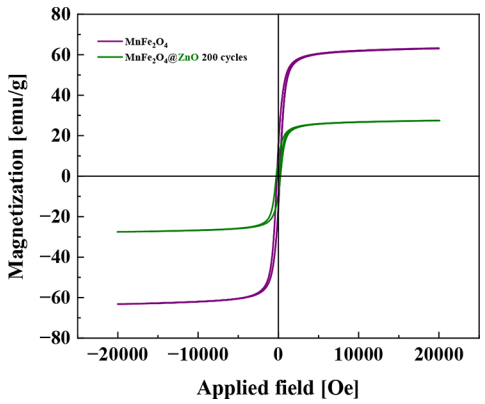

Figure 7. M vs H hysteresis loop at room temperature for $MnFe_2O_4$ magnetic nanoparticles and the $MnFe_2O_4$@ZnO nanocomposite material.

is observed, with saturation magnetization (M_s) values of 63 emu g^{-1} for $MnFe_2O_4$ and 27 emu g^{-1} for $MnFe_2O_4$@ZnO, along with coercivity (H_c) values of 186 and 260 Oe, respectively. The coercivity being close to zero relative to the applied external magnetic field indicates that the $MnFe_2O_4$ nanoparticles exhibit characteristics of a soft magnetic material. This implies that the material can be easily magnetized and demagnetized, as evidenced by its low coercive field and the increase in magnetization until saturation is reached. The low coercivity observed suggests that both $MnFe_2O_4$ and $MnFe_2O_4$@ZnO nanoparticles behave similarly to superparamagnetic materials. This behavior is characterized by a significant number of magnetic moments aligning with the external magnetic field, contributing to the net magnetization of the material in the presence of an applied field. Assuming that the fabricated magnetic nanoparticles are monocrystalline, the magnetic properties of $MnFe_2O_4$ can be correlated with particle and crystallite sizes, which were determined through XRD and TEM. The relationship between particle size and magnetic properties indicates a tendency toward superparamagnetic behavior characterized by reduced coercivity and enhanced saturation magnetization. This correlation is crucial for applications requiring precise control over the magnetic properties of nanoparticles, in this case, the magnetic separation process in wastewater environmental remediation.

3.5. Photodegradation Test. After coating the magnetic cores with 200 cycles of DEZ precursor to generate an ultrathin film of ZnO, the photocatalytic activity was tested by monitoring the Red Amaranth dye concentration every 30 min by examining the intensity of the absorbance peak at 520 nm with a UV−visible spectrophotometer, as shown in Figure 8, to observe the photodegradation process. Figure 8a−d corresponds to the control sample (only AZO dye without photocatalyst), ZnO film sample immersed in AZO dye solution, $MnFe_2O_4$ magnetic cores without the ZnO layer, and the magnetic cores surface coated with ZnO layer via ALD. By comparing these plots, there is an evident peak intensity decrease as time passes during sampling for the sample with the ZnO layer. However, the sample without the ZnO layer on the magnetic cores presents a negligible intensity loss after 240 min under UV irradiation compared with the control sample (Red Amaranth without photocatalyst). To assess the influence of the ZnO layer on the photodegradation process, the ultrathin film deposited on the silicon substrate used as a witness and placed in the ALD reactor during the coating of the magnetic cores process was placed into the quartz cuvette with AZO dye. Following this, the photocatalysis experiment was performed under identical experimental conditions (sampling time, power UV light, etc.), enabling a direct comparison of its photocatalytic performance with that of the composite material.[75] The results of this experiment indicated that just the ZnO film in contact with the dye did not exhibit a significant effect on dye degradation compared with the impact on the dye due to the ZnO layer coating on the surface of magnetic cores. Figure 8e shows the normalized absorbance spectra under UV−vis radiation with the photocatalyst synthesized from the magnetic nanoparticles; the photodegradation continued over 4 h, resulting in a degradation efficiency η_{eff} around 60%.

The degradation efficiency was determined using the following relation:

$$\eta = \frac{C_0 - C_t}{C_0} \times 100 = \frac{A_0 - A_t}{A_0} \times 100 \quad (1)$$

where A_0 corresponds to the initial absorbance for the dye mixture and A_t is the absorbance at t time, respectively; both values are related to the initial concentration, C_0, as well as the concentration C_t at t time, following the Lambert−Beer law. The designed magneto-controlled photocatalyst successfully degraded Red Amaranth dye, which is a common pollutant in the textile and food industries. Photocatalytic degradation tests demonstrated the potential of this material for scalable applications in water remediation. The material is environmentally friendly, taking advantage of the magnetic properties of Manganese ferrite cores and the photoactive features provided by the ZnO ultrathin coating on the cores. Additionally, the magnetic core could enable the photocatalyst to be easily recovered from water by using an external magnetic field, facilitating its reuse via a magnetic separation

https://doi.org/10.1021/acsomega.4c11468
ACS Omega 2025, 10, 17595−17610

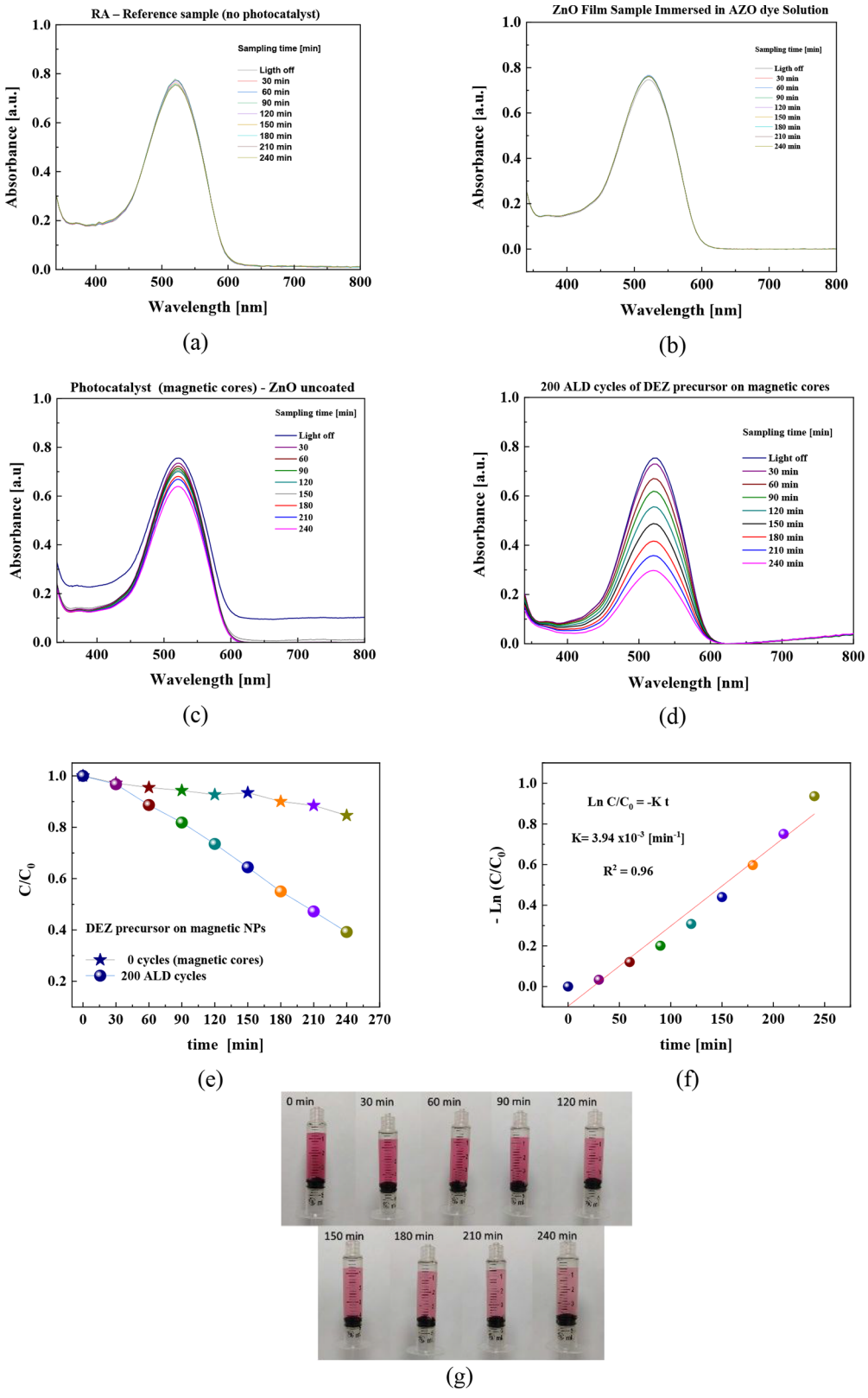

Figure 8. Absorbance spectra for $MnFe_2O_4$@ZnO (a) RA control sample without photocatalyst, (b) ZnO film sample immersed in AZO dye solution, (c) magnetic nanoparticles without ZnO coating, and (d) magnetic nanoparticles coated with ZnO by ALD. (e) Normalized absorbance spectra under UV−vis radiation with the photocatalyst synthesized from the magnetic nanoparticles, (f) photodegradation kinetics of Amaranth dye, (g) gradual color fading for Red Amaranth dye up to 240 min of exposure.

process that can be implemented in industrial water-treatment processes.

Photodegradation kinetics was evaluated using the equation

$$\mathrm{Ln}\frac{A_t}{A_0} = -Kt \tag{2}$$

https://doi.org/10.1021/acsomega.4c11468
ACS Omega 2025, 10, 17595−17610

where A_0 and A_t denote the absorbance values before and after UV irradiation at time t during the photocatalytic process, respectively, and K [min $^{-1}$] is the rate constant. The K value was obtained by fitting the experimental data in Figure 8f using linear regression analysis based on eq 2. The K constant represents the reaction rate, and the photocatalytic kinetics determine the dye degradation rate, following a pseudo-first-order kinetic model. The corresponding K value for the decolorization process was approximately 3.94×10^{-3} min $^{-1}$, considering data every 30 min during 240 min under a UV−vis light source. Figure 8g demonstrates the systematic decolorization of Red Amaranth throughout the experiment, with the solution gradually transitioning from an intense red to progressively lighter shades. This color change serves as a visual indicator of the dye's progressive degradation under photocatalytic conditions. The fading of color corresponds to the breakdown of the azo dye molecules as the active photocatalyst facilitates the reduction in dye concentration. Decolorization is particularly pronounced with an increasing irradiation time, confirming the effectiveness of the photocatalytic process. This visual representation highlights the nanocomposite fabricated efficiency in promoting dye degradation, further supported by quantitative data in Figure 8a−c. To evaluate the mineralization degree of Red Amaranth dye at the end of the reaction, the total organic carbon parameter was determined, which indicates the level of organic carbon converted to inorganic carbon (CO_2). The results indicate (Figure 9) a TOC conversion of 2.3 and 34.1% for

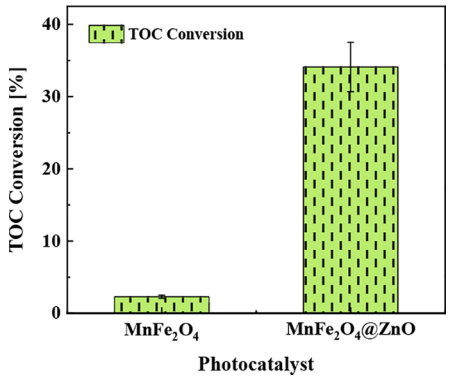

Figure 9. TOC (%) measured after the end of reaction (240 min) for $MnFe_2O_4$ magnetic nanoparticles and the $MnFe_2O_4$@ZnO nanocomposite material.

$MnFe_2O_4$ and $MnFe_2O_4$@ZnO, respectively. It is worth noting that the TOC conversion obtained with the $MnFe_2O_4$@ZnO photocatalyst is like or even above other studies previously reported where this dye is used as a model molecule, or analogous materials are employed to eliminate other dyes (see Table 2).

The organic carbon content of the solution was determined by total organic carbon (TOC) measurement using a spectrometer (Hach DR2800, method 10129), and the TOC conversion was calculated according to the following equation:

$$\%\text{TOC Conversion} = \left(1 - \frac{\text{Organic carbon content}}{\text{Organic carbon initial}}\right) \times 100 \quad (3)$$

In addition, the optical band gap of a photoactive material is a critical parameter in photodegradation tests, as it dictates the material's ability to absorb light and generate charge carriers essential for photocatalytic reactions. In our study, the bandgap energy (E_g) of the ZnO film deposited on magnetic cores was determined from absorbance data, obtaining a value close to 3.19 eV, calculated using the Tauc−Lorentz model, which is widely used for the optical characterization of semiconductors and dielectrics. The 3.19 eV bandgap value for ZnO is consistent with typical values reported in the literature, although it may vary slightly depending on morphology, synthesis method, and experimental conditions. It is well-known that the Tauc-Lorentz model combines Tauc's equation, used to determine the bandgap in amorphous and polycrystalline semiconductors, with the Lorentz model, which describes the dielectric response. For a first-order transition (allowed direct transition), the relationship between the absorption coefficient α and the photon energy $h\nu$.[85] Figure 10 depicts the band gap obtained using the Tauc model, in this case, to determine the 3.19 eV band gap value, $(\alpha E)^2$ was plotted as a function of E. A linear fit was applied to the linear region of the curve to obtain the slope and intercept values. Finally, this fitted line was extrapolated to the energy axis to determine the E_g value.

As discussed before, knowing the optical band gap value is essential for understanding the photocatalytic behavior of the ZnO layer. This is relevant in the photodegradation process, where the efficiency of light absorption directly influences charge carrier generation and reactive species formation. Photodegradation process schemes using the $MnFe_2O_4$@ZnO nanoparticles are shown in Figure 11. The photodegradation mechanism for our nanocomposite begins when light, from the source, is absorbed by the ZnO layer deposited on a magnetic nanoparticle, promoting electrons from the valence band to the conduction band. The transferred

Table 2. Comparison of AZO Dye Degradation Using Different Photocatalysts: Correlation between Degradation Performance and the TOC Percentage

photocatalyst	concentration	dye	degradation [%]	TOC [%]	time [h]	reference
TiO_2 P-25/Cu	10 [mg/L]	O−II	97	89	9	76
Fe- TiO_2	3 [g/L]	AO7	80	73	1	77
TiO_2@Fe_3O_4	5 [mg/L]	MB	66.6	48.21	10	78
ZnO/$MnFe_2O_4$	5 [mg/L]	MB	85%	71.5	4	79
TiO_2 thin films	no report	AY	40	74.46	24	80
TiO2 - ZrO2	10 [mg/L]	RhB	78.1	74.3	3	81
Sm-doped ZnO	236 [mg/L]	CR	84.5	no report	4	82
SnP@ZnO	50 [mg/L]	AM	41	78	1	83
ZnO	no report	AM	74	no report	7	84

https://doi.org/10.1021/acsomega.4c11468
ACS Omega 2025, 10, 17595−17610

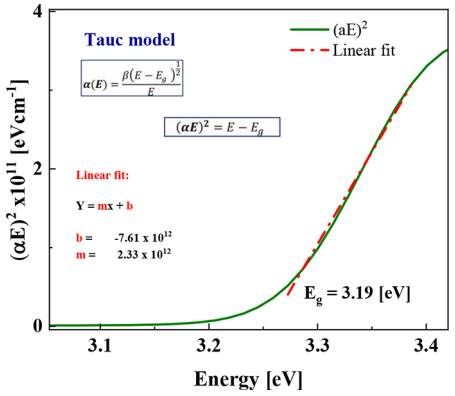

Figure 10. Estimation of the optical bandgap energy using the Tauc–Lorentz model.

electrons reduce oxygen molecules to form superoxide anions (O_2^-), while the holes oxidize water or hydroxide ions to generate hydroxyl radicals (OH). These reactive species degrade organic pollutants like Amaranth dye into smaller molecules such as CO_2 and H_2O.[86,87]

3.6. Theoretical Approximation. The enhanced photodegradation efficiency of ZnO-coated $MnFe_2O_4$ nanoparticles, compared to pure $MnFe_2O_4$ nanoparticles, can be qualitatively explained by examining numerical simulations of their absorbance and scattering cross sections, as shown in Figure 12a. The extinction cross-section, which combines absorbance and scattering, provides a numerical approximation of the experimental UV–vis absorbance measurements. In these calculations, performed with nanoparticles in water (refractive index = 1.33), all data are normalized to the maximum extinction value of the ZnO-coated $MnFe_2O_4$ nanoparticles. Results are presented with solid lines for ZnO-coated $MnFe_2O_4$ and dashed-dotted lines for uncoated nanoparticles. In uncoated nanoparticles, absorbance (associated with optical losses) is the primary factor determining extinction and exhibits a monotonic decrease, accompanied by a small shoulder (due to the optical resonance of the dielectric nanoparticle) around 500 nm. In contrast, for the coated nanoparticles, scattering (due to the strong dipole resonance of the nanocube) dominates along the entire spectrum of the study, with a sharp peak around 400 nm. To further understand the experimentally observed photodegradation, from an electromagnetic point of view, we simulated near-fields at wavelengths relevant to Red Amaranth strong absorption peak around 520 nm (Figure 8c,d). Figure 12b depicts the near-field for uncoated $MnFe_2O_4$ nanoparticles, revealing an enhanced dipole-like field around the nanoparticle surface. This field results from absorption due to optical losses in the $MnFe_2O_4$ material, which only modestly contributes to photodegradation, as shown in Figure 8c.

In the case of ZnO-coated $MnFe_2O_4$ nanoparticles, the near-field at 365 nm, shown in Figure 12c, demonstrates significant field enhancement due to light scattering associated with a strong dipole resonance. Additionally, Figure 12d shows the near field at 520 nm, where the enhanced and localized fields at the ZnO-medium interface contribute to a stronger light-matter interaction. These enhanced near-fields polarize the environment surrounding nanoparticles, along with the high absorption by the inner $MnFe_2O_4$ nanoparticles (see Figure 12c), are key factors that enhance the photodegradation performance of ZnO-coated $MnFe_2O_4$ nanoparticles in the degradation of Red Amaranth. This phenomenon is further illustrated in Figure 13a,b, which present the normalized electric field profiles along the *xz*-plane at the middle of the nanocubes. While the resonant electromagnetic field at 520 nm exhibits a slightly lower amplitude than at 365 nm, where the field is predominantly concentrated at the ZnO outer surface, it displays a more distributed nature. The 520 nm field extends across both the inner and outer interfaces of the ZnO-coated $MnFe_2O_4$ structure, exhibiting a slower decay with an increasing distance from the nanoparticle. Although the presence of interfering ions (not considered in this study) may hinder the degradation of certain pollutants,[80] such effects cannot be fully captured by the electromagnetic simulations conducted here.

4. CONCLUSIONS

In this study, $MnFe_2O_4$ nanoparticles were synthesized using a hydrothermal method and subsequently coated with a ∼36 nm layer of ZnO via atomic layer deposition, forming $MnFe_2O_4$@ZnO as a photoactive material. A detailed examination of their structural, morphological, and magnetic properties, along with their photodegradation performance, was conducted. Crystallographic analyses confirmed the formation of a spinel structure associated with manganese ferrite magnetic cores. Additionally, a hexagonal wurtzite phase, characteristic of the ZnO coating, was observed on the $MnFe_2O_4$@ZnO samples. The crystallite size of the magnetic nanoparticles was determined to be 36.5 ± 0.2 nm, while the overall nanoparticle size was measured to be 33.2 ± 9.1 nm. Comparative analysis showed that both the uncoated and ZnO-coated nanoparticles exhibited a tendency toward superparamagnetic behavior at room temperature, as indicated by a minor hysteresis loop. However, the ZnO-coated magnetic cores displayed a reduction in saturation magnetization (in emu/g), attributed to the presence of the ZnO semiconductor layer. It can be

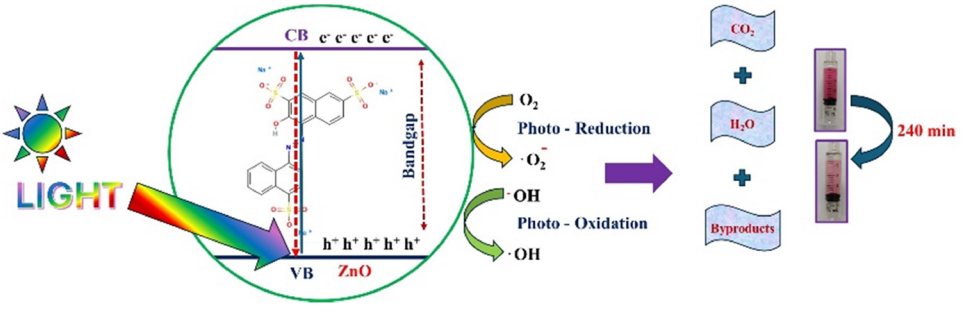

Figure 11. Photodegradation scheme process for the $MnFe_2O_4$@ZnO nanocomposite.

https://doi.org/10.1021/acsomega.4c11468
ACS Omega 2025, 10, 17595−17610

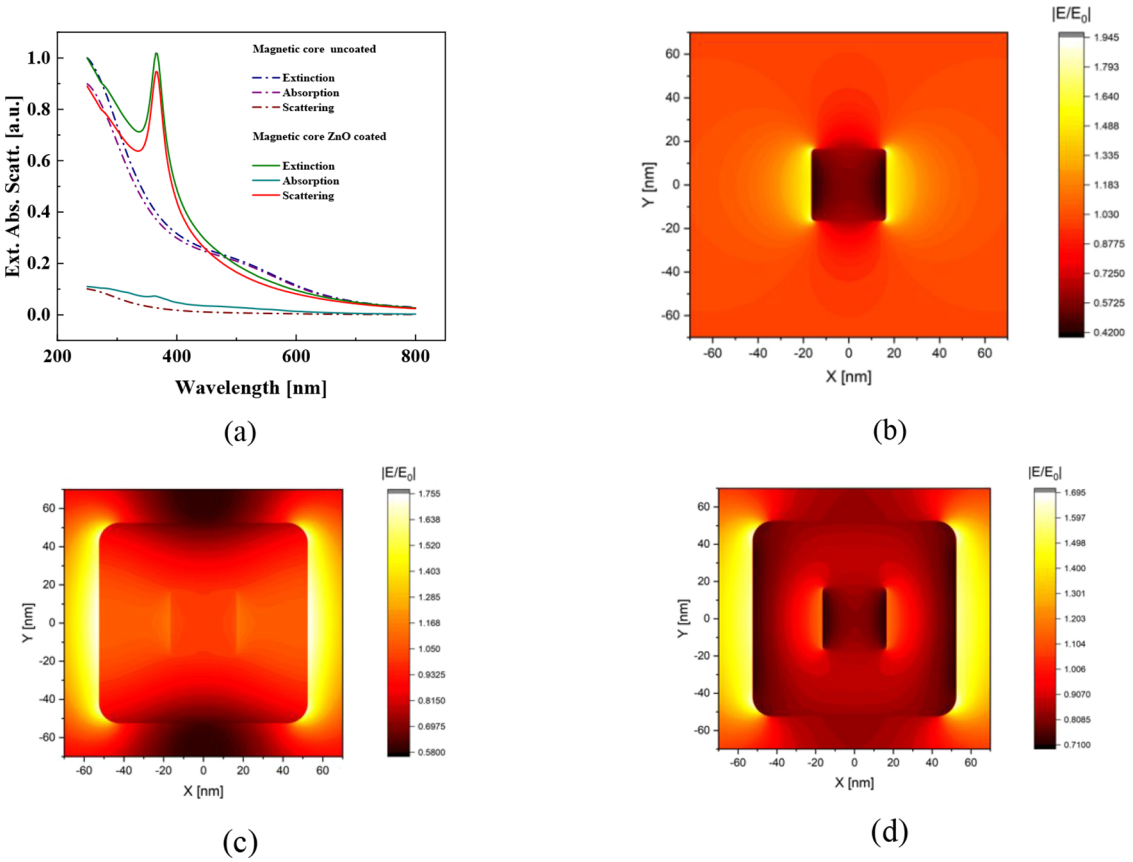

Figure 12. (a) Normalized extinction, scattering, and absorption spectra for the ZnO-coated (solid lines) and uncoated (dash-dot-dot lines) $MnFe_2O_4$ nanoparticles. (b) Near-field for a $MnFe_2O_4$ nanoparticle around 520 nm. (c) and (d) Near-fields for the ZnO-coated $MnFe_2O_4$ nanoparticles, calculated at 365 and 520 nm, respectively.

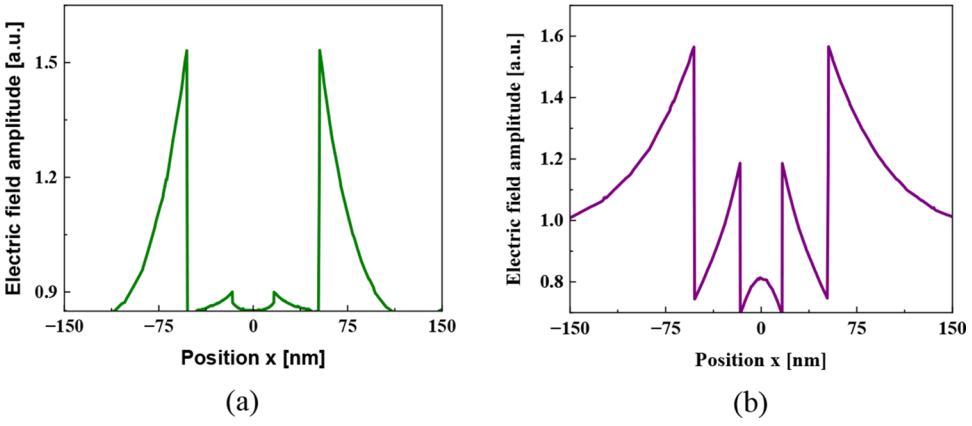

Figure 13. Normalized electric field profiles along the *xz*-plane for $MnFe_2O_4$@ZnO nanocubes calculated at (a) 365 and (b) 520 nm, respectively.

asserted that the $MnFe_2O_4$@ZnO nanocomposite-based photocatalyst is a multifunctional material, as it combines the photocatalytic activity provided by the ALD-deposited ZnO coating with the magnetic response of the nanoparticles. Our study demonstrated that the photocatalytic and magnetic properties of this system were effective in degrading Red Amaranth azo dye, highlighting the potential to explore various magnetic materials coated with photoactive layers using the ALD technique. The results showed that the ZnO coating on the magnetic cores achieved a degradation efficiency of nearly 60% for the toxic Red Amaranth dye solution after 240 min. Finite-difference time-domain (FDTD) electromagnetic simulations were conducted to further support these findings. Overall, the results indicate that the $MnFe_2O_4$@ZnO nanocomposite can be classified as a soft magnetic and multifunctional material, with significant potential for photocatalytic applications combined with magnetic separation processes, offering an eco-friendly alternative for wastewater treatment.

■ ASSOCIATED CONTENT

Data Availability Statement

The data supporting this study's findings are presented throughout the manuscript. The corresponding data can be visualized in OriginPro 2023 by clicking on each graph. To

https://doi.org/10.1021/acsomega.4c11468
ACS Omega 2025, 10, 17595−17610

clarify, this study does not include additional supplementary files. Further details regarding the experimental procedures and analytical methods can be provided by the corresponding author, J.A.L.M., upon reasonable request.

AUTHOR INFORMATION

Corresponding Author

Javier Alonso Lopez Medina − *SECIHTI - IxM - Centro de Nanociencias y Nanotecnología, Universidad Nacional Autónoma de México, Ensenada, B.C. C.P. 22800, México;* orcid.org/0009-0006-2146-5511; Email: javierlo21@ens.cnyn.unam.mx

Authors

David Domínguez − *Centro de Nanociencias y Nanotecnología, Universidad Nacional Autónoma de México, Ensenada, B.C. C.P. 22800, México*

Pedro Pizá − *Centro de Investigación en Materiales Avanzados−CIMAV, Chihuahua, CH C.P. 31136, México*

Guoduan Liu − *Materials and Manufacturing Technology-University of California, Irvine, California C.P. 92697-3975, United States*

Camilo Velez − *Department of Mechanical and Aerospace Engineering, University of California, Irvine, California C.P. 92697-3975, United States*

Faustino Reyes Gómez − *National Institute of Telecommunications (Inatel), Santa Rita do Sapucaí C.P. 37536-001, Brazil;* orcid.org/0000-0001-5758-0489

Mario Humberto Farías − *Centro de Nanociencias y Nanotecnología, Universidad Nacional Autónoma de México, Ensenada, B.C. C.P. 22800, México*

Uriel Caudillo-Flores − *Centro de Nanociencias y Nanotecnología, Universidad Nacional Autónoma de México, Ensenada, B.C. C.P. 22800, México;* orcid.org/0000-0002-2492-8407

Gerardo Soto Herrera − *Centro de Nanociencias y Nanotecnología, Universidad Nacional Autónoma de México, Ensenada, B.C. C.P. 22800, México*

Hugo Tiznado − *Centro de Nanociencias y Nanotecnología, Universidad Nacional Autónoma de México, Ensenada, B.C. C.P. 22800, México;* orcid.org/0000-0002-4068-1889

Jorge Ricardo Mejía-Salazar − *National Institute of Telecommunications (Inatel), Santa Rita do Sapucaí C.P. 37536-001, Brazil;* orcid.org/0000-0003-1742-9957

Complete contact information is available at: https://pubs.acs.org/10.1021/acsomega.4c11468

Author Contributions

J.A.L.M.: Investigation, Formal analysis, Conceptualization, Methodology, Visualization, Writing - original draft, Visualization, Project administration. D.D.: Investigation, Methodology, Visualization, Writing−original draft. P.P.: Visualization, Validation, Resources, Writing−original draft. C.V.C.: Visualization, Supervision, Writing - review and editing, G.L.: Conceptualization, Visualization, Writing−review and editing. F.R.G.: Investigation, Formal analysis, Visualization, Software, Writing - review and editing. M.H.F.: Writing - review and editing, Supervision, Funding acquisition. U.C.F.: Visualization, Methodology, Writing - review and editing. G.S.H.: Writing - original draft, Visualization, Supervision, Funding acquisition. H.T.: Conceptualization, Supervision, Writing - review and editing. J.R.M.S.: Investigation, Formal analysis, Visualization. Writing - original draft.

Funding

The National Autonomous University of Mexico (UNAM) covered the open-access publication fee for this article through an existing agreement with the journal. This agreement provides funding for the article processing charge (APC) for authors with UNAM affiliation, when the corresponding author uses an email address ending in @···unam.mx. This work was partially supported by Dirección General de Asuntos del Personal Académico (DGAPA) de la UNAM, through research projects: PAPIIT IN110424, IA100624, IG101124, IN116424, IG100925, IN112922. The authors acknowledge the use of facilities and instrumentation at the UC Irvine Materials Research Institute (IMRI), supported in part by the National Science Foundation Materials Research Science and Engineering Center program through the UC Irvine Center for Complex and Active Materials (DMR-2011967). This work also was partially supported by the Brazilian agencies FAPEMIG (APQ-05305-23) and RNP, with resources from MCTIC, Grant No. 01245.020548/2021-07, under the Brazil 6G project of the Radiocommunication Reference Center (Centro de Referência em Radiocomunicações-CRR) of the National Institute of Telecommunications (Instituto Nacional de Telecomunicações-Inatel), Brazil.

Notes

The authors declare no competing financial interest.

ACKNOWLEDGMENTS

The authors would like to thank the valuable technical support offered by the Magnetic Microsystems and Microrobotics group at the University of California, Irvine; also, by Francisco Ruiz, Eloisa Aparicio, Israel Gradilla, Eduardo Murillo, Luis Alejandro Arce Saldaña, Luis Pérez C., and Naji Tarabay. J. Lopez−Medina acknowledges support from the SECIHTI Program via Investigadores por México through Project 146-2016.

REFERENCES

(1) Jaikumar, V.; Pavithra, K. G. Removal of Colorants from Wastewater: A Review on Sources and Treatment Strategies. *J. Ind. Eng. Chem.* **2019**, *75*, 1−19.

(2) Singh, B. J.; Chakraborty, A.; Sehgal, R. A Systematic Review of Industrial Wastewater Management: Evaluating Challenges and Enablers. *J. Environ. Manage.* **2023**, *348* (June), No. 119230.

(3) Periyasamy, A. P. Recent Advances in the Remediation of Textile-Dye-Containing Wastewater: Prioritizing Human Health and Sustainable Wastewater Treatment. *Sustainability* **2024**, *16* (2), 495.

(4) Mustafa, S. A.; Al-Rudainy, A. J.; Salman, N. M. Effect of Environmental Pollutants on Fish Health: An Overview. *Egypt. J. Aquat. Res.* **2024**, *50* (2), 225−233.

(5) Alsukaibi, A. K. D. Various Approaches for the Detoxification of Toxic Dyes in Wastewater. *Processes* **2022**, *10* (10), 1968.

(6) Mukherjee, A. G.; Wanjari, U. R.; Eladl, M. A.; El-Sherbiny, M.; Elsherbini, D. M. A.; Sukumar, A.; Kannampuzha, S.; Ravichandran, M.; Renu, K.; Vellingiri, B.; Kandasamy, S.; Gopalakrishnan, A. V. Mixed Contaminants: Occurrence, Interactions, Toxicity, Detection, and Remediation. *Molecules* **2022**, *27* (8), 2577.

(7) Barciela, P.; Perez-Vazquez, A.; Prieto, M. A. Azo Dyes in the Food Industry: Features, Classification, Toxicity, Alternatives, and Regulation. *Food Chem. Toxicol.* **2023**, *178* (July), No. 113935.

(8) Chung, K. T. Azo Dyes and Human Health: A Review. *J. Environ. Sci. Heal. - Part C Environ. Carcinog. Ecotoxicol. Rev.* **2016**, *34* (4), 233−261.

(9) Rehman, K.; Ashraf, A.; Azam, F.; Hamid Akash, M. S. Effect of Food Azo-Dye Tartrazine on Physiological Functions of Pancreas and Glucose Homeostasis. *Turkish J. Biochem.* **2019**, *44* (2), 197−206.

(10) Sin, J. C.; Lam, S. M.; Mohamed, A. R.; Lee, K. T. Degrading Endocrine Disrupting Chemicals from Wastewater by TiO2 Photocatalysis: A Review. *Int. J. Photoenergy* **2012**, *2012*, 1−23.
(11) Imtiazuddin, S. M.; Tiki, A. Textile Azo Dyes; Significance, Ecological, Health, and Safety Issues. *Pakistan J. Chem.* **2021**, *10* ((1−4)), 35−38.
(12) dos Santos, J. R.; de Sousa Soares, L.; Soares, B. M.; de Gomes Farias, M.; de Oliveira, V. A.; de Sousa, N. A. B.; Negreiros, H. A.; da Silva, F. C. C.; Peron, A. P.; Pacheco, A. C. L.; Marques, M. M. M.; Gonçalves, J. C. R.; Montenegro, R. C.; Islam, M. T.; Sharifi-Rad, J.; Mubarak, M. S.; de Melo Cavalcante, A. A. C.; de Castro E Sousa, J. M. Cytotoxic and Mutagenic Effects of the Food Additive Tartrazine on Eukaryotic Cells. *BMC Pharmacol. Toxicol.* **2022**, *23* (1), 1−10.
(13) Maheshwari, K.; Agrawal, M.; Gupta, A. B. Dye Pollution in Water and Wastewater BT. In *Novel Materials for Dye-Containing Wastewater Treatment*; Springer: Singapore, 2021.
(14) Kaur, N. Different Treatment Techniques of Dairy Wastewater. *Groundw. Sustain. Dev.* **2021**, *14* (July), No. 100640.
(15) Jabbar, Z. H.; Esmail Ebrahim, S. Recent Advances in Nano-Semiconductors Photocatalysis for Degrading Organic Contaminants and Microbial Disinfection in Wastewater: A Comprehensive Review. *Environ. Nanotechnol. Monit. Manag.* **2022**, *17*, No. 100666.
(16) Jain, K.; Patel, A. S.; Pardhi, V. P.; Flora, S. J. S. Nanotechnology in Wastewater Management: A New Paradigm towards Wastewater Treatment. *Molecules* **2021**, *26* (6), 1797.
(17) Shekho, M. S.; Hassan, N. E. A Review on Techniques for the Cleaning of Wastewater. *GSC Adv. Res. Rev.* **2024**, *18* (1), 118−128.
(18) Xie, Y.; Hu, J.; Esmaeili, H.; Wang, D.; Zhou, Y. A Review Study on Wastewater Decontamination Using Nanotechnology: Performance, Mechanism and Environmental Impacts. *Powder Technol.* **2022**, *412*, No. 118023.
(19) Santos, M. C.; Antonin, V. S.; Souza, F. M.; Aveiro, L. R.; Pinheiro, V. S.; Gentil, T. C.; Lima, T. S.; Moura, J. P. C.; Silva, C. R.; Lucchetti, L. E. B.; Codognoto, L.; Robles, I.; Lanza, M. R. V. Decontamination of Wastewater Containing Contaminants of Emerging Concern by Electrooxidation and Fenton-Based Processes−A Review on the Relevance of Materials and Methods. *Chemosphere* **2022**, *307*, No. 135763.
(20) Rashid, R.; Shafiq, I.; Akhter, P.; Iqbal, M. J.; Hussain, M. A State-of-the-Art Review on Wastewater Treatment Techniques: The Effectiveness of Adsorption Method. *Environ. Sci. Pollut. Res.* **2021**, *28* (8), 9050−9066.
(21) Khan, A.; Ju, P.; Han, Z.; Ni, C. A Comprehensive Review on Adsorptive Removal of Azo Dyes Using Functional Materials. *Aqua Water Infrastructure, Ecosyst. Soc.* **2024**, *73* (2), 266−285.
(22) Ren, G.; Han, H.; Wang, Y.; Liu, S.; Zhao, J.; Meng, X.; Li, Z. Recent Advances of Photocatalytic Application in Water Treatment: A Review. *Nanomaterials* **2021**, *11* (7), 1804.
(23) Karim, A. V.; Krishnan, S.; Shriwastav, A. An Overview of Heterogeneous Photocatalysis for the Degradation of Organic Compounds: A Special Emphasis on Photocorrosion and Reusability. *J. Indian Chem. Soc.* **2022**, *99* (6), No. 100480.
(24) Friedmann, D. A General Overview of Heterogeneous Photocatalysis as a Remediation Technology for Wastewaters Containing Pharmaceutical Compounds. *Water (Switzerland)* **2022**, *14* (21), 3588.
(25) Pelosato, R.; Bolognino, I.; Fontana, F.; Sora, I. N. Applications of Heterogeneous Photocatalysis to the Degradation of Oxytetracycline in Water: A Review. *Molecules* **2022**, *27* (9), 2743.
(26) Ahmed, S. N.; Haider, W. Heterogeneous Photocatalysis and Its Potential Applications in Water and Wastewater Treatment: A Review. *Nanotechnology* **2018**, *29* (34), 342001.
(27) Antonopoulou, M. Homogeneous and Heterogeneous Photocatalysis for the Treatment of Pharmaceutical Industry Wastewaters: A Review. *Toxics* **2022**, *10* (9), 539.
(28) Nie, C.; Dong, J.; Sun, P.; Yan, C.; Wu, H.; Wang, B. An Efficient Strategy for Full Mineralization of an Azo Dye in Wastewater: A Synergistic Combination of Solar Thermo- and Electrochemistry plus Photocatalysis. *RSC Adv.* **2017**, *7* (58), 36246−36255.
(29) Ajith, M. P.; Aswathi, M.; Priyadarshini, E.; Rajamani, P. Recent Innovations of Nanotechnology in Water Treatment: A Comprehensive Review. *Bioresour. Technol.* **2021**, *342*, No. 126000.
(30) Mathur, J.; Goswami, P.; Gupta, A.; Srivastava, S.; Minkina, T.; Shan, S.; Rajput, D. V. Nanomaterials for Water Remediation: An Efficient Strategy for Prevention of Metal(Loid) Hazard. *Water (Switzerland)* **2022**, *14* (24), 3998.
(31) Malik, S.; Muhammad, K.; Waheed, Y. Nanotechnology: A Revolution in Modern Industry. *Molecules* **2023**, *28* (2), 661.
(32) Wang, G. Nanotechnology: The New Features. *arXiv:1812.04939* 2018, .
(33) Ke, C. Recent Advances in Nanotechnology. *Int. J. Nanomater. Nanotechnol. Nanomed.* **2011**, *9*, 015−023.
(34) Gupta, D.; Varghese, B. S.; Suresh, M.; Panwar, C.; Gupta, T. K. *Nanoarchitectonics: Functional Nanomaterials and Nanostructures—a Review*; Springer: Netherlands, 2022; Vol. *24*.
(35) Leonel, A. G.; Mansur, A. A. P.; Mansur, H. S. Advanced Functional Nanostructures Based on Magnetic Iron Oxide Nanomaterials for Water Remediation: A Review. *Water Res.* **2021**, *190*, No. 116693.
(36) Castriciano, M. A. Functional Nanostructures for Sensors, Optoelectronic Devices, and Drug Delivery. *Nanomaterials* **2020**, *10* (6), 1195.
(37) Basso, C. R.; Crulhas, B. P.; Castro, G. R.; Pedrosa, V. A. Recent Advances in Functional Nanomaterials for Diagnostic and Sensing Using Self-Assembled Monolayers. *Int. J. Mol. Sci.* **2023**, *24* (13), 10819.
(38) López, J.; Ortíz, A. A.; Muñoz-Muñoz, F.; Dominguez, D.; Díaz de León, J. N.; Galindo, J. T. E.; Hogan, T.; Gómez, S.; Tiznado, H.; Soto-Herrera, G. Magnetic Nanostructured Based on Cobalt−Zinc Ferrites Designed for Photocatalytic Dye Degradation. *J. Phys. Chem. Solids* **2021**, *150*, No. 109869.
(39) Wu, S.; Hu, W.; Ze, Q.; Sitti, M.; Zhao, R. Multifunctional Magnetic Soft Composites: A Review. *Multifunct. Mater.* **2020**, *3* (4), No. 042003.
(40) Kuncser, V. Multifunctional Magnetic Nanocomposites: Innovative Processing and Applications. *Nanomaterials* **2023**, *13* (1), 206.
(41) Vasić, K.; Knez, Ž.; Leitgeb, M. Multifunctional Iron Oxide Nanoparticles as Promising Magnetic Biomaterials in Drug Delivery: A Review. *J. Funct. Biomater.* **2024**, *15* (8), 227.
(42) López Medina, J. A.; Domínguez, D.; Tarabay, N.; Velez, C.; Pizá Ruiz, P.; Aguila, S. A.; Guerrero Sanchez, J.; Sharma, S.; Farías, M. H.; Soto Herrera, G.; Ponce Perez, R. Magnetic, Structural, and Morphological Properties Behavior of Ni1−XCoxFe2O4Magnetic Nanoparticles: Theoretical and Experimental Study. *Mater. Charact.* **2024**, *216*, No. 114296.
(43) Vedrtnam, A.; Kalauni, K.; Dubey, S.; Kumar, A. A Comprehensive Study on Structure, Properties, Synthesis and Characterization of Ferrites. *AIMS Mater. Sci.* **2020**, *7* (6), 800−835.
(44) Boutra, B.; Güy, N.; Özacar, M.; Trari, M. Magnetically Separable MnFe2O4/TA/ZnO Nanocomposites for Photocatalytic Degradation of Congo Red under Visible Light. *J. Magn. Magn. Mater.* **2020**, *497*, No. 165994.
(45) Selima, S. S. Structural, Magnetic, Optical Properties and Photocatalytic Activity of Nanocrystalline Cobalt Ferrite Prepared by Three Different Methods. *Biointerface Res. Appl. Chem.* **2021**, *12* (1), 1335−1351.
(46) Jadhav, S. A.; Somvanshi, S. B.; Khedkar, M. V.; Patade, S. R.; Jadhav, K. M. Magneto-Structural and Photocatalytic Behavior of Mixed Ni−Zn Nano-Spinel Ferrites: Visible Light-Enabled Active Photodegradation of Rhodamine B. *J. Mater. Sci. Mater. Electron.* **2020**, *31* (14), 11352−11365.
(47) Jacinto, M. J.; Ferreira, L. F.; Silva, V. C. Magnetic Materials for Photocatalytic Applications—a Review. *J. Sol-Gel Sci. Technol.* **2020**, *96* (1), 1−14.

https://doi.org/10.1021/acsomega.4c11468
ACS Omega 2025, 10, 17595−17610

(48) Garcia-Muñoz, P.; Fresno, F.; de la Peña O'Shea, V. A.; Keller, N. *Ferrite Materials for Photoassisted Environmental and Solar Fuels Applications*; Springer International Publishing, 2020; Vol. *378*.
(49) Kurian, M.; Thankachan, S. Structural Diversity and Applications of Spinel Ferrite Core - Shell Nanostructures- A Review. *Open Ceram.* **2021**, *8*, No. 100179.
(50) Kefeni, K. K.; Mamba, B. B.; Msagati, T. A. M. Application of Spinel Ferrite Nanoparticles in Water and Wastewater Treatment: A Review. *Sep. Purif. Technol.* **2017**, *188*, 399−422.
(51) Ramadoss, G.; Suriyaraj, S. P.; Sivaramakrishnan, R.; Pugazhendhi, A.; Rajendran, S. Mesoporous Ferromagnetic Manganese Ferrite Nanoparticles for Enhanced Visible Light Mineralization of Azoic Dye into Nontoxic By-Products. *Sci. Total Environ.* **2021**, *765*, No. 142707.
(52) Sotelo, D. C.; Ornelas-Soto, N.; Osma, J. F. Novel Magnetic Polymeric Filters with Laccase-Based Nanoparticles for Improving Congo Red Decolorization in Bioreactors. *Polymers (Basel)* **2022**, *14* (12), 2328.
(53) Taghavi Fardood, S.; Moradnia, F.; Mostafaei, M.; Afshari, Z.; Faramarzi, V.; Ganjkhanlu, S. Biosynthesis of MgFe2 O4Magnetic Nanoparticles and Their Application in Photodegradation of Malachite Green Dye and Kinetic Study. *Nanochem. Res.* **2019**, *4* (1), 86−93.
(54) Rodiah, S.; Ditiyaningrum, C. O. Plant-Mediated Green Synthesis of Nanoparticles NiCoFe2O4 Photocatalyst Using Africa Leaves Infusion. *J. Akad. Kim.* **2022**, *11* (3), 146−152.
(55) Wang, J.; Yang, J.; Li, X.; Wang, D.; Wei, B.; Song, H.; Li, X.; Fu, S. Preparation and Photocatalytic Properties of Magnetically Reusable Fe3O4@ZnO Core/Shell Nanoparticles. *Phys. E Low-Dimensional Syst. Nanostructures* **2016**, *75*, 66−71.
(56) Wang, H.; Yao, Q.; Wang, C.; Ma, Z.; Sun, Q.; Fan, B.; Jin, C.; Chen, Y. Hydrothermal Synthesis of Nanooctahedra MnFe2O4 onto the Wood Surface with Soft Magnetism, Fire Resistance and Electromagnetic Wave Absorption. *Nanomaterials* **2017**, *7* (6), 118.
(57) Ma, Y.; Xu, X.; Lu, L.; Meng, K.; Wu, Y.; Chen, J.; Miao, J.; Jiang, Y. Facile Synthesis of Ultrasmall MnFe2O4 Nanoparticles with High Saturation Magnetization for Magnetic Resonance Imaging. *Ceram. Int.* **2021**, *47* (24), 34005−34011.
(58) Gan, Y. X.; Jayatissa, A. H.; Yu, Z.; Chen, X.; Li, M. Hydrothermal Synthesis of Nanomaterials. *J. Nanomater.* **2020**, *2020*, 1−3.
(59) Cai, J.; Ma, Z.; Wejinya, U.; Zou, M.; Liu, Y.; Zhou, H.; Meng, X. A Revisit to Atomic Layer Deposition of Zinc Oxide Using Diethylzinc and Water as Precursors. *J. Mater. Sci.* **2019**, *54* (7), 5236−5248.
(60) Yang, J.; Bahrami, A.; Ding, X.; Lehmann, S.; Kruse, N.; He, S.; Wang, B.; Hantusch, M.; Nielsch, K. Characteristics of ALD-ZnO Thin Film Transistor Using H2O and H2O2 as Oxygen Sources. *Adv. Mater. Interfaces* **2022**, *9* (15), 1−9.
(61) Seong, S.; Jung, Y. C.; Lee, T.; Park, I. S.; Ahn, J. Fabrication of Fe3O4-ZnO Core-Shell Nanoparticles by Rotational Atomic Layer Deposition and Their Multi-Functional Properties. *Curr. Appl. Phys.* **2016**, *16* (12), 1564−1570.
(62) Zhang, J.; Li, Y.; Cao, K.; Chen, R. Advances in Atomic Layer Deposition. *Nanomanufacturing Metrol.* **2022**, *5* (3), 191−208.
(63) Kafshgari, L. A.; Ghorbani, M.; Azizi, A. Synthesis and Characterization of Manganese Ferrite Nanostructure by Co-Precipitation, Sol-Gel, and Hydrothermal Methods. *Part. Sci. Technol.* **2019**, *37* (7), 904−906.
(64) Cuadra, J. G.; Abderrahim Lahlahi, S. P.; Cadena, R.; Santiago Toca, D. F.; Carda, J. Zinc Oxide Thin Films: Synthesis and Photocatalytic Applications. In *Intech - Nanotechnology and Nanomaterials Annual*; IntechOpen, 2016; Vol. *2021*, p. 13.
(65) Krajian, H.; Abdallah, B.; Kakhia, M.; AlKafri, N. Hydrothermal Growth Method for the Deposition of ZnO Films: Structural, Chemical and Optical Studies. *Microelectron. Reliab.* **2021**, *125*, No. 114352.
(66) Gençyılmaz, O. Hydrothermal Synthesis of ZnO Films and Characterization. *Anadolu Univ. J. Sci. Technol. A - Appl. Sci. Eng.* **2016**, *17*, 660.
(67) Poddighe, M.; Innocenzi, P. Hydrophobic Thin Films from Sol−Gel Processing: A Critical Review. *Materials (Basel).* **2021**, *14* (22), 6799.
(68) Sengupta, J.; Sahoo, R. K.; Bardhan, K. K.; Mukherjee, C. D. Influence of Annealing Temperature on the Structural, Topographical and Optical Properties of Sol-Gel Derived ZnO Thin Films. *Mater. Lett.* **2011**, *65* (17−18), 2572−2574.
(69) Di Mauro, A.; Fragalà, M. E.; Privitera, V.; Impellizzeri, G. ZnO for Application in Photocatalysis: From Thin Films to Nanostructures. *Mater. Sci. Semicond. Process.* **2017**, *69* (March), 44−51.
(70) Zhang, M. W.; Lin, K. Y. A.; Huang, C. F.; Tong, S. Enhanced Degradation of Toxic Azo Dye, Amaranth, in Water Using Oxone Catalyzed by MIL-101-NH2 under Visible Light Irradiation. *Sep. Purif. Technol.* **2019**, *227*, 115632.
(71) López-Medina, J.; Carvalho, W. O. F.; Vazquez-Arce, J.; Moncada-Villa, E.; Oliveira, O. N.; Farías, M. H.; Tiznado, H.; Mejía-Salazar, J. R. Refractive Index of ZnO Ultrathin Films Alternated with Al2O3 in Multilayer Heterostructures. *Nanotechnology* **2020**, *31* (50), 505715.
(72) Wang, X.; Lee, E.; Xu, C.; Liu, J. High-Efficiency, Air-Stable Manganese−Iron Oxide Nanoparticle-Pigmented Solar Selective Absorber Coatings toward Concentrating Solar Power Systems Operating at 750 °C. *Mater. Today Energy* **2021**, *19*, No. 100609.
(73) Desai, H. B.; Hathiya, L. J.; Joshi, H. H.; Tanna, A. R. Synthesis and Characterization of Photocatalytic MnFe2O4 Nanoparticles. *Mater. Today Proc.* **2020**, *21*, 1905−1910.
(74) Kim, M. G.; Kang, J. M.; Lee, J. E.; Kim, K. S.; Kim, K. H.; Cho, M.; Lee, S. G. Effects of Calcination Temperature on the Phase Composition, Photocatalytic Degradation, and Virucidal Activities of TiO2Nanoparticles. *ACS Omega* **2021**, *6* (16), 10668−10678.
(75) Di Mauro, A.; Cantarella, M.; Nicotra, G.; Privitera, V.; Impellizzeri, G. Low Temperature Atomic Layer Deposition of ZnO: Applications in Photocatalysis. *Appl. Catal. B Environ.* **2016**, *196*, 68−76.
(76) Divya, N.; Bansal, A.; Jana, A. K. Photocatalytic Degradation of Azo Dye Orange II in Aqueous Solutions Using Copper-Impregnated Titania. *Int. J. Environ. Sci. Technol.* **2013**, *10* (6), 1265−1274.
(77) Mancuso, A.; Sacco, O.; Sannino, D.; Pragliola, S.; Vaiano, V. Enhanced Visible-Light-Driven Photodegradation of Acid Orange 7 Azo Dye in Aqueous Solution Using Fe-N Co-Doped TiO2. *Arab. J. Chem.* **2020**, *13* (11), 8347−8360.
(78) Li, Z.; Li, L.; Zhang, S.; Zhang, L.; Cui, Y.; Shi, H. Ultrasound Assisted TiO2@Fe3O4 Nanocomposites Photocatalytic Degradation of Organic Pollutants in Potato Starch Processing Wastewater. *Sep. Purif. Technol.* **2024**, *332*, No. 125799.
(79) Akshhayya, C.; Swedha, M.; Elgorban, A. M.; Bahkali, A. H.; Varma, R. S.; Younus, M.; Balakrishnaraja, R.; Syed, A.; Khan, S. S. Intimate Coupling of 3D MnFe2O4 Cubes on 1D ZnO Nanorods for Sustainable Photocatalysis under Visible Light: Computational Analysis of Reactive Sites and Degradation Pathway. *J. Taiwan Inst. Chem. Eng.* **2022**, *141* (March), No. 104558.
(80) Tiwari, D.; Lalhriatpuia, C.; Lalhmunsiama; Lee, S. M.; Kong, S. H. Efficient Application of Nano-TiO 2 Thin Films in the Photocatalytic Removal of Alizarin Yellow from Aqueous Solutions. *Appl. Surf. Sci.* **2015**, *353*, 275−283.
(81) Ruîz-Santoyo, V.; Marañon-Ruiz, V. F.; Romero-Toledo, R.; Gonzâlez Vargas, O. A.; Pêrez-Larios, A. Photocatalytic Degradation of Rhodamine B and Methylene Orange Using TiO2-ZrO2 as Nanocomposite. *Catalysts* **2021**, *11*, 1035.
(82) Pascariu, P.; Cojocaru, C.; Olaru, N.; Samoila, P.; Airinei, A.; Ignat, M.; Sacarescu, L.; Timpu, D. Novel Rare Earth (RE-La, Er, Sm) Metal Doped ZnO Photocatalysts for Degradation of Congo-Red Dye: Synthesis, Characterization and Kinetic Studies. *J. Environ. Manage.* **2019**, *239*, 225−234.

https://doi.org/10.1021/acsomega.4c11468
ACS Omega 2025, 10, 17595−17610

(83) Shee, N. K.; Kim, H. J. Surface Modification of ZnO with Sn(IV)-Porphyrin for Enhanced Visible Light Photocatalytic Degradation of Amaranth Dye. *Molecules* **2023**, *28* (18), 6481.
(84) Torres-Torres, K.; Nash-Montes, V. I.; Luciano-Velázquez, J.; Bailón-Ruiz, S. J. Degradation of Amaranth and Tropaeolin O in the Presence of ZnO Nanoparticles. *Int. Nano Lett.* **2022**, *12* (3), 295−300.
(85) López, J.; Solorio, E.; Borbón-Nuñez, H. A.; Castillón, F. F.; Machorro, R.; Nedev, N.; Farías, M. H.; Tiznado, H. Refractive Index and Bandgap Variation in Al2O3-ZnO Ultrathin Multilayers Prepared by Atomic Layer Deposition. *J. Alloys Compd.* **2017**, *691*, 308−315.
(86) Al-Mamun, M. R.; Iqbal Rokon, M. Z.; Rahim, M. A.; Hossain, M. I.; Islam, M. S.; Ali, M. R.; Bacchu, M. S.; Waizumi, H.; Komeda, T.; Hossain Khan, M. Z. Enhanced Photocatalytic Activity of Cu and Ni-Doped ZnO Nanostructures: A Comparative Study of Methyl Orange Dye Degradation in Aqueous Solution. *Heliyon* **2023**, *9* (6), No. e16506.
(87) Almohamadi, H.; Awad, S. A.; Sharma, A. K.; Fayzullaev, N.; Chiguala-contreras, L.; Amari, A.; Rodriguez-benites, C. Photocatalytic Activity of Metal- and Non-Metal-Anchored ZnO and TiO2 Nanocatalysts for Advanced Photocatalysis: Comparative Study. *Catalysts* **2024**, *14* (420), 420.

https://doi.org/10.1021/acsomega.4c11468
ACS Omega 2025, 10, 17595−17610